

An open-source, distributed workflow for band mapping data in multidimensional photoemission spectroscopy

R. Patrick Xian^{1,7}, Yves Acremann², Steinn Y. Agustsson³, Maciej Dendzik¹, Kevin Bühlmann², Davide Curcio⁴, Dmytro Kutnyakhov^{5,7}, Federico Pressacco⁶, Michael Heber⁵, Shuo Dong¹, Jure Demsar³, Wilfried Wurth^{5,6}, Philip Hofmann⁴, Martin Wolf¹, Laurenz Rettig^{1,7}, and Ralph Ernstorfer^{1,7}

¹Fritz Haber Institute of the Max Planck Society, Berlin, Germany

²Department of Physics, ETH Zurich, Switzerland

³Department of Physics, University of Mainz, Mainz, Germany

⁴Department of Physics, Aarhus University, Aarhus, Denmark

⁵DESY Photon Science, Hamburg, Germany

⁶Department of Physics, University of Hamburg, Hamburg, Germany

⁷Corresponding authors: xian@fhi-berlin.mpg.de, rettig@fhi-berlin.mpg.de, ernstorfer@fhi-berlin.mpg.de

Abstract

Characterization of the electronic band structure of solid state materials is routinely performed using photoemission spectroscopy. Recent advancements in short-wavelength light sources and electron detectors give rise to multidimensional photoemission spectroscopy, which permits parallel measurements of the electron spectral function in energy, two momentum components and additional physical parameters with single-event detection capability. Processing the photoelectron event streams with a rate of a few to tens of megabytes per second poses a major data challenge in the field. We describe an open-source, distributed workflow for efficient interaction with single-electron events in photoemission band mapping experiments compatible with beamlines at 3rd and 4th generation light sources as well as table-top laser sources. The workflow transforms single-event data into calibrated and structured formats for subsequent storage, visualization and further analysis by facility users. The workflow can be archived for reuse and provides a basis for the documentation and comparison of multidimensional band mapping data and their integration into materials science databases.

1 Introduction

Many disciplines in the natural sciences are increasingly dealing with densely sampled multidimensional datasets. The scientific workflows to obtain and process them is becoming increasingly complex due to the provenance and structure of the data and the information needed to be extracted [1, 2]. In materials science and condensed matter physics, various spectroscopic and structural characterization techniques produce experimental data of distinct formats and characteristics. Their creation and understanding require customized processing and analysis pipelines designed by specialists in the respective fields. The growing incentive for building experimental materials science databases [3] that complement established theoretical counterparts [4] calls for open-source and reusable data workflows [5, 6] that bring raw data to shareable formats for downstream access, analysis and comparison by non-specialists of the experimental techniques [7, 8]. Among the various properties associated with materials, the electronic band structure (EBS) of condensed matter systems is of vital importance to the understanding of their electronic properties in and out of equilibrium. Multidimensional photoemission spectroscopy (MPES) [9, 10, 11] is an emerging technique that offers high-throughput EBS characterization through band mapping experiments and holds promise as an enabling technology for building experimental EBS databases, where data integration requires traceable knowledge of the processing steps between the archived and the raw format. Here we present an open-source data workflow that focuses on this aspect for band mapping data from MPES. In the following, we briefly introduce the technology of MPES and the associated data processing, before providing details on the data workflow.

MPES, also called the momentum microscopy (MM), is born out of the recent integration of time-of-flight (TOF) electron spectrometers with delay-line detectors (DLDs) and improved electron-optic lens designs [12, 13, 14, 15]. Compared with the earlier generations of angle-resolved photoemission spectroscopy (ARPES) [16, 17, 18] that uses a hemispherical analyzer to measure the 2D energy-momentum distribution of the photoemitted electrons [19], MPES is capable of recording single-electron events simultaneously sorted into the (k_x, k_y, E) coordinates (E : electron energy, k_x, k_y : parallel momentum components) in band mapping experiments, obviating the need for scanning across sample orientations and data merging as is the case for similar experiments based on ARPES. Operation of the TOF DLD in MPES requires a pulsed photon source and is directly compatible with 3rd and 4th generation light sources [20] as well as laboratory-based table-top setups [21, 22, 23, 24], harnessing their high repetition rates in the range of multi-kilohertz to megahertz to drastically improve the detection speed and efficiency. Mapping of the 3D band structure with sufficient signal-to-noise ratio (SNR) may be achieved on the timescale of minutes. The technological convergence opens up the possibilities to record 3D datasets in dependence of one or more additional parameters, such as probe photon energy, $I(k_x, k_y, E, k_z)$ [10], spin-polarization, $I(k_x, k_y, E, S)$

[9], or pump-probe time in time-resolved MM, $I(k_x, k_y, E, t)$ [25] within a reasonable time frame.

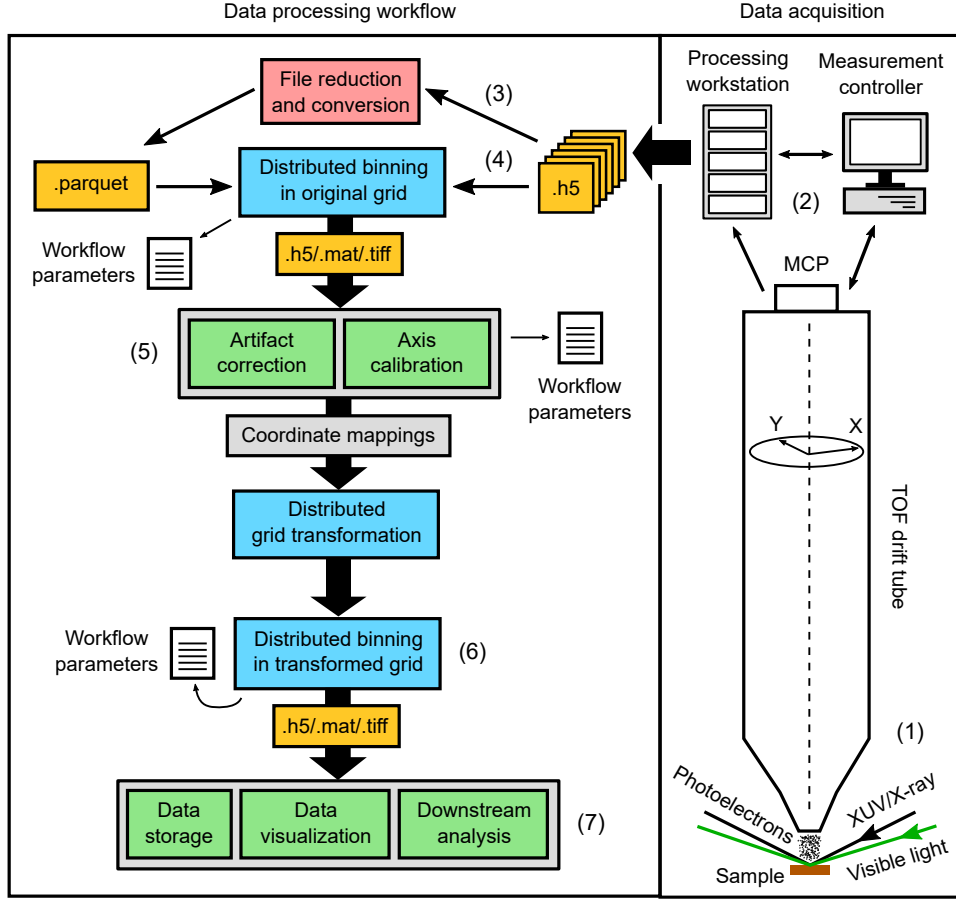


Figure 1: **Schematic of the workflow in MPES.** The data acquisition in MPES starts from (1) photoelectrons liberated by the extreme UV (XUV) or X-ray photons travelling through the lens systems and the TOF tube to trigger detection events on the multichannel plate (MCP). (2) Single-event data acquisition is monitored and controlled by the measurement controller computer. The raw data are first streamed and stored into hard drive in HDF5 format (.h5) and subsequently processed in the workflow through (3) file reduction (optional), (4)(6) distributed binning, (5) artifact correction and axis calibrations, carried out at the single-event or the binned data levels. At the end of the workflow, other data formats are generated (such as HDF5, MAT or TIFF) for (7) storage, visualization or downstream analysis for extracting relevant physical parameters. Critical parameters within the workflow may be exported (as workflow parameters files) and shared reuse for processing other datasets.

From the data perspective, the pulsed sources with high repetition rates generate densely sampled data at rates of multiple megabytes per second (MB/s), which has brought about challenges in data processing and management compared with conventional ARPES experiments. The raw data in MPES are single photoelectron events registered by the DLD and the physical quantities related to the detected events are streamed in parallel to the storage files

in a hierarchical file format (e.g. HDF5 [26]). A typical dataset involves $10^7 - 10^{10}$ detected events with a total size of several to a few hundred of gigabytes (GBs), depending on the number of coordinates measured (3D or 4D) and the required SNR. Unlike the large 2D or 3D image-based datasets, such as those obtained in various forms of light [27, 28] and electron microscopies [29, 30], processing and conversion of tabulated single-event data requires additional steps of statistical computing for conversion into standard images. This motivation underlies the current workflow development for efficient data processing and analysis. In data processing and calibration, experiments at different facilities share similar procedures going from the raw events to the multidimensional hypervolume with calibrated axes, which is the basis for archiving and downstream analysis. To maintain reproducibility for the particular data source and structure, we have summarized the workflow (see Fig. 1) into two open-source software packages (`hextof-processor` [31] and `mpes` [32]), with similar design principles for coping with large facility and table-top experiments, respectively. The core of our approach includes distributed statistical processing at the single-event level using parameters calibrated and determined from preprocessed volumetric datasets, which enables effective instrument diagnostics, artifact correction, and sample condition monitoring. The algorithms involved balance physical knowledge and existing methods in image processing and computer vision. The workflow is illustrated next with data originated from some of the electron momentum microscopes currently in operation, such as the HEXTOF (high energy X-ray time-of-flight) measurement system [25] at the free-electron laser source FLASH [33] at DESY, and the table-top high harmonic generation-based setup at the Fritz Haber Institute [22] involving a commercial TOF and DLD (METIS 1000, SPECS GmbH). We expect the workflow described here to serve as a blueprint for upcoming software platforms in similar setups to be installed in other facilities or laboratories worldwide.

2 Results

2.1 Workflow overview

Workflow description. The workflow schematic shown in Fig. 1 starts with raw single-event data from measurements. The data are (1) binned in a distributed fashion in the measurement coordinate system, including the photoelectron’s position on the detector (X, Y), its TOF, a digital encoder (ENC) axis, and others if four or more dimensions are acquired in parallel. The binned histogram is (2) used for estimation of the numerical transforms for distortion correction and axis calibration. Next, the transforms are (3) applied to the raw single-event data to convert the measurement coordinate system to the physical axes, (k_x, k_y, E, t_{pp}) and others for four or higher dimensions (see also Fig. 2). Finally, the single-event data are (4) binned in the transformed grid to yield 3D, 3D+t or other higher-dimensional data with the correct

axis values. The outcome may be exported in different formats for storage, visualization and downstream analysis.

Tasks and softwares. Processing billion-count single-event data requires user interaction for data checking and distributed processing to reduce the time consumption. The general tasks in the workflow include the transformation of data streams to multidimensional histogram, artifact correction and axis calibration. These operations can be efficiently decomposed into column-wise operations of the distributed dataframe format offered by the `dask` package [34] in Python. While the use of `dask` dataframe provides the common foundation for interactivity with single events of `hextof-processor` and `mpes`, they distinguish themselves by the experimental requirements. At large facilities, experiments often record a large number of machine parameters that need to be stored, though only a small number of relevant parameters are needed for downstream processing. Therefore, the `hextof-processor` package includes a parameter sampling step to retrieve intermediate tabulated data in the Apache Parquet format, a column-based data structure optimized for computational efficiency [35]. This approach reduces the processing overhead in searching through the raw files every time when data are queried during the subsequent processing. As an open-source project, other beamtime-specific functionalities are added by users to the existing framework at every new experimental run. The `mpes` package adapts to the much simpler file structure produced at table-top experimental setups and makes direct use of the HDF5 raw data. It comes with added functionalities motivated by the existing issues encountered in data acquisition and downstream processing such as axis calibration, masking, alignment and different forms of artifact correction.

2.2 Workflow components

Artifact correction

Artifacts in MPES data come from the mechanical imperfections, stray field (electric and magnetic), uncertainties in the alignment of sample, light beams and the multistage electron-optic lens systems as well as the data digitization process. Minimizing the effects of instrumental imperfections plays an important role in the downstream analysis. Artifact correction is carried out sequentially at the level of single photoelectron events or the data hypervolume from multidimensional histogramming (see Fig. 2).

Digitization artifact. The time-to-digital converter (TDC) outputs digitized data according to the binning width of the on-board electronics. Data conversion from one digitized format to another in a rebinning process often creates a picket fence-like effect. This phenomenon originates from the incommensurate bin size in the two rounds of sampling processes (binning and rebinning). To solve the problem, one introduces a slight amount of uniformly distributed noise with an amplitude equal or less than half of the bin size to the single-event values when

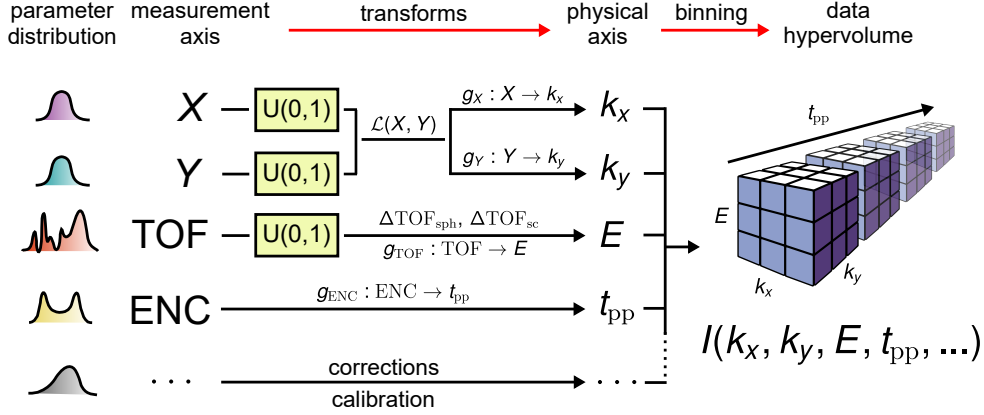


Figure 2: **Examples of workflow components.** Illustrations are given for artifact correction and axis calibration. Characteristic 1D distributions of the measured X , Y , TOF, ENC and an arbitrary axis are shown on the very left. $U(0, 1)$ represent uniformly distributed random noise added to suppress digitization artifacts (jittering or dithering). The transforms (g 's) are calibration functions that convert the values in the measurement axes to the physical ones. The transform $\mathcal{L}(X, Y)$ corrects the symmetry distortion, while the spherical timing aberration and space charge are compensated for by $\Delta\text{TOF}_{\text{sph}}$ and $\Delta\text{TOF}_{\text{sc}}$, respectively. Binning of the corrected single-event data over the calibrated physical axes yields a multidimensional hypervolume (right picture) of photoemission intensity data along with the physical axes values.

calculating the bin counts. This is similar to the histogram jittering (or dithering) technique [36, 37] used in statistical visualization and computer graphics. Mathematically, the uniformly distributed noise $U(0, 1)$ bounded in the range $[0, 1]$ is added before binning a univariate data stream, $S = \{S_i\}$ via,

$$S'_i = S_i + \frac{w_b}{2} \times U(0, 1). \quad (1)$$

Here, w_b is the bin width. For binning of multivariate data streams, such as the detector X position (or k_x), Y position (or k_y), and the photoelectron TOF (or E), we adopt the same approach individually for each dimension. The effect of jittering in reducing the digitization artifact is shown in Fig. 3.

Spherical timing aberration. Electrons entering the TOF tube at different lateral positions travel through different path lengths to reach the detector, which is the origin of the spherical timing aberration as illustrated in Fig. 4. The lateral position-dependent time delay may be expressed as,

$$\Delta\text{TOF}_{\text{sph}}(r) = (\sqrt{1 + r^2/d^2} - 1)\text{TOF}_0, \quad (2)$$

where r is the radial distance from the center of the DLD and TOF_0 is the TOF normalization constant. For a typical field-free region length of $d \sim 1$ m in the TOF tube and a DLD screen radius of $r = 50$ mm, $\Delta\text{TOF}/\text{TOF}_0 \approx 1.25 \times 10^{-3}$. Assuming $\text{TOF}_0 = 0.5 \mu\text{s}$, the spherical timing aberration in TOF scale is $\Delta\text{TOF}_{\text{sph}} \approx 0.62$ ns, which is larger than the DLD's

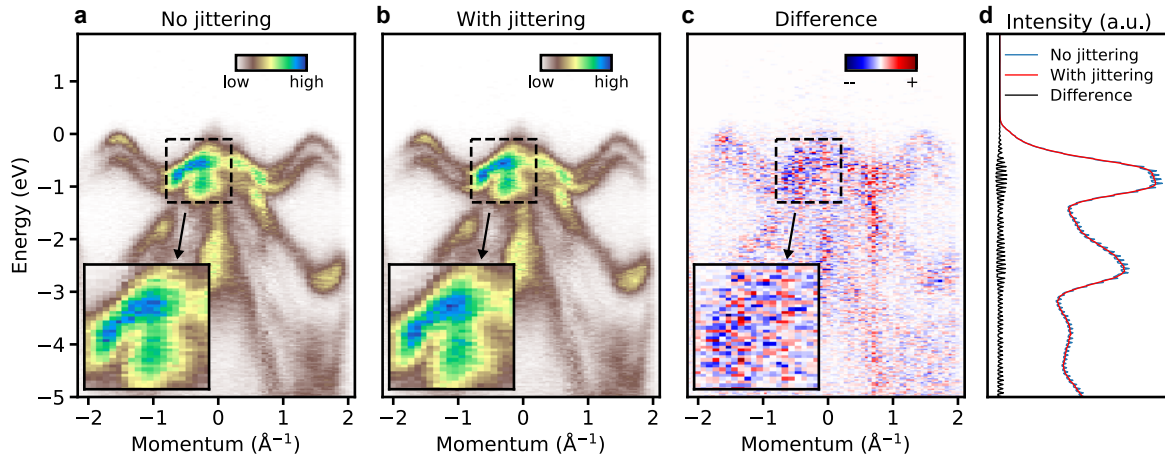


Figure 3: **Digitization artifact correction by histogram jittering.** Removal of the digitization artifact is illustrated with a 2D k - E slice across the Brillouin zone center of the band mapping dataset measured at FHI on WSe_2 . The images before and after histogram jittering and their difference are shown in **a**, **b** and **c** respectively. A zoomed-in section of the data are shown in the insets in **a-c**. The effective removal of the digitization artifact is further demonstrated in the momentum-integrated energy distribution curves in **d**. The traces in **d** are computed by averaging horizontally over their corresponding 2D images in **a-c**.

temporal resolution of ~ 0.15 ns. The effect of the spherical timing aberration is visible for a few eV energy range with fine bins but quite small on a large energy range. To illustrate this effect, we use the $\text{W}4f$ core-level data presented in Fig. 4b. For every (X, Y) position on the detector the peak of $\text{W}4f_{7/2}$ was fitted with a Voigt profile and the peak positions are shown in Fig. 4c. As core-level spectra of heavy elements don't show dispersion, the deviation from fitting corresponds to the spherical timing aberration of the electron optics. In order to compensate for the spherical timing aberration, we first transform the data from Cartesian to the polar coordinates (see Fig. 4c), and then fit the radial-averaged peak position to a polynomial function of the radius,

$$\Delta\text{TOF}_{\text{sph}}(r) = \frac{r^2\text{TOF}_0}{2d^2} - \frac{r^4\text{TOF}_0}{8d^4} + \text{O}(r^6). \quad (3)$$

The fitting results together with the corrected radial distribution are presented in Fig. 4d.

Symmetry distortion. Photoemission patterns in the (k_x, k_y) plane (i.e. an energy slice) may exhibit distorted symmetry due to the influence of various factors from the instrument, the sample and the experimental geometry on the trajectory of low-energy photoelectrons. Correction of the symmetry distortion yet preserving the intensity features requires the use of symmetry-related landmarks to solve for the symmetrization coordinate transform in the framework of nonrigid image registration [38]. In typical situations with a good electron lens

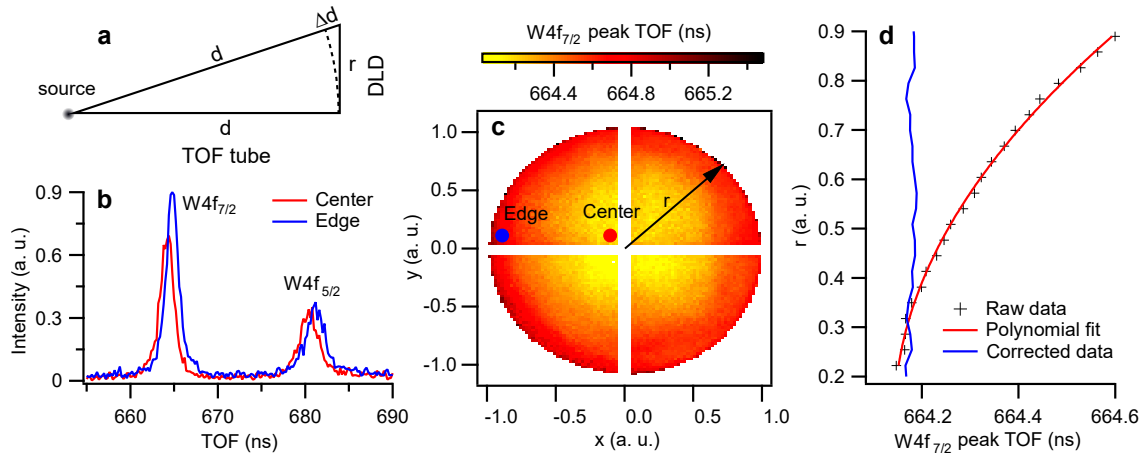


Figure 4: **Spherical timing aberration correction.** The correction is demonstrated using W4f core-level data measured at FLASH. **a.** Illustration of the geometric origin of the spherical timing aberration in the time-of-flight (TOF) drift tube. **b.** Comparison of the W4f spectra at the center and on the edge of the detector plane. The energy spectra are extracted from the corresponding regions, marked by the dots in the same blue and red colors, respectively, in **c.** The white stripes crossing at the detector center block the exposed edges of the four-quadrant detector quadrants. **d.** The uncorrected and corrected radial-averaged peak TOF positions for the W4f_{7/2} core level.

alignment, the energy dependence of the momentum distortion within the focused phase space volume covering an energy range of several eV is negligible, so the same coordinate transform can be applied to all energy slices in the volumetric data (including valence and conduction bands) or simultaneously to all single events.

Other single-volume artifacts. (1) Momentum center shift: The momentum center of the emergent photoelectron through the electron-optic system may experience an energy-dependent shift owing to slight misalignment in the system or stray fields. Correction of the center shift requires an energy-dependent center alignment of energy slices. The shift along the energy or TOF axis may be estimated using phase correlation [39] or mutual information-based [40] sequential image registration methods, in which the series of energy slices is treated as an image sequence. In a well-shielded and well-aligned electron-optic lens system, generally, the momentum center shift is negligible in the focused photoelectron energy range. (2) Space-charge effect (SCE): The space charges from the probe and pump pulses cause a “doming effect” of the photoemission intensity distribution around the momentum center of the band structure. This is especially visible in systems with a clear Fermi edge [9, 11] or non-dispersing shallow core levels, which may be used as references for calibrating the parameters used for the flattening transform by applying a momentum-dependent shift $\Delta\text{TOF}_{\text{sc}}(k_x, k_y)$ in the TOF (or the calibrated energy) coordinate of the single-event data.

Axis calibration

To transform the measurement axes of the DLD into physical axes relevant for electronic band mapping, several calibrations are required, as shown in Fig. 2. The calibration functions are constructed with parameters derived from comparing physical knowledge of the materials (e.g. Brillouin zone size, Fermi level position) with data. They are applied either to the data hypervolume or to the single-electron events raw data individually in a distributed fashion before binning.

Momentum calibration. The scaling factors for momentum calibration are computed by comparing the positions of known high symmetry points in the band structure with their corresponding locations in an energy slice. Suppose A and B are two high symmetry points identifiable (e.g. as local extrema) from the experimental data with pixel positions (X_A, Y_A) and (X_B, Y_B) , and momentum positions, (k_x^A, k_y^A) and (k_x^B, k_y^B) , respectively. We calculate the pixel-to-momentum scaling ratios, f_X and f_Y , along the X (column) and Y (row) directions of a 2D k -space image, respectively. Then, the momentum coordinate (k_x, k_y) at each pixel position (X, Y) may be derived.

$$f_D = (k_d^A - k_d^B)/(D_A - D_B) \quad (4)$$

$$k_d = f_D \times (D - D_A) \quad (D, d = X, x \text{ or } Y, y) \quad (5)$$

Energy calibration. The calibration requires a set of band mapping data measured at different bias voltages, usually sampled with a spacing of 0.5 V in a range of ± 3 -5 V around the normally applied bias voltage for a particular sample. The calibration proceeds by finding the TOF feature (e.g. local extrema) correspondences in the 1D energy distribution curves (EDCs) at different biases using the dynamic time warping algorithm [41]. The transformation from the TOF to the photoelectron energy E is approximated as a polynomial function,

$$E(\text{TOF}) = \sum_{i=0}^n a_i \text{TOF}^i \quad (6)$$

The approximation is valid within a range of ~ 20 eV, sufficient for the range covering the entire valence band and some low-lying conduction bands of typical materials. The polynomial coefficients is determined using nonlinear least squares by solving $\Delta T \cdot \mathbf{a} = \Delta E$, in which $\mathbf{a} = (a_1, a_2, \dots)^T$ is the coefficient vector while the constant offset a_0 is determined by manual alignment to the Fermi level. The vector ΔE and the matrix ΔT contain, respectively, the pairwise differences of the bias voltages and the polynomial terms of differential TOF values. To calibrate a large energy range including multiple core levels, a piecewise polynomial may be used [11].

Pump-probe delay calibration. The time origin ('time zero') in time-resolved photoemission spectroscopy, i.e. the temporal overlap of pump and probe pulses, is determined by fitting of a characteristic trace extracted from the data. Since the readings of the digital encoder are sampled linearly, equally-spaced pump-probe delays are directly convertible from the readings using linear interpolation, given the boundary values of the translation stage positions and the corresponding delay times. For unequally-spaced delays, a delay marker is first added to each data point as a separate column after data acquisition to group together the encoder reading ranges that correspond to the specific time delays. The data binning is carried out over the delay marker column instead of the equally-sampled encoder readings.

2.3 Workflow extension

Data storage. The simplistic form of the output data hypervolume derived from single-electron events includes non-negative scalar values of the photoemission intensity and the calibrated real-valued axes coordinates, including k_x , k_y , E , and other parameter dependencies such as the pump-probe time delay t_{pp} . The values are exported as HDF5, MAT or TIFF. For the HDF5 format [26], the photoemission intensities and axis values are stored as HDF5 datasets, while the metadata are included as attributes of the files.

Data visualization. Scientific visualization in the physical sciences [42, 43] offers an array of methods for handling various forms of data, most of which can be realized in existing open-source softwares such as matplotlib [44], ParaView [42] and Blender [45]. Their adaptation to band mapping data from MPES requires to incorporate the needs and knowledge of the data characteristics in this domain. The band mapping data in 3D (multi-megavoxel) and 3D+t (multi-gigavoxel) include inherent symmetries from the electronic band structure and localized features in the spatial, intensity, temporal and other domains that disrupt the perfect symmetry. The overall goal is to emphasize these features of interest while exploiting the symmetry components to simplify the visualization.

We discuss here three methods for the display of volumetric band mapping data, which are, at the same time, the basis for visualizing 3D+t data with time as an animated axis. (1) The orthoslice representation includes orthogonal 2D planes selected in specific regions in the volume [42], which highlights specific slices deep within the data less visible in a volumetrically rendered view (see Fig. 5a). Along this line, we have developed a software package, 4Dview [46], to explore 4D data using simultaneously linked orthoslices, which also features contrast adjustment and data integration within a hypervolume of interest. (2) The band path plot is a 2D representation of the 3D band mapping volume generated by combining a series of 2D cuts along sampled momentum paths (or k-paths) traversing a list of so-called high-symmetry points [47, 48]. This representation captures the largest dispersion within the band structure.

For volumetric data, the same path may be sampled from all the energy coordinates to produce the plot shown in Fig. 5b. The analysis and visualization modules in the `mpes` package include functionalities to compose customized band path plots. (3) The cut-out view exposes a specific part of interest in the volumetric data, while not losing the rest (see Fig. 5c) [42]. The analysis module in the `mpes` package provides ways to generate precise cut-out using position landmarks and inequalities.

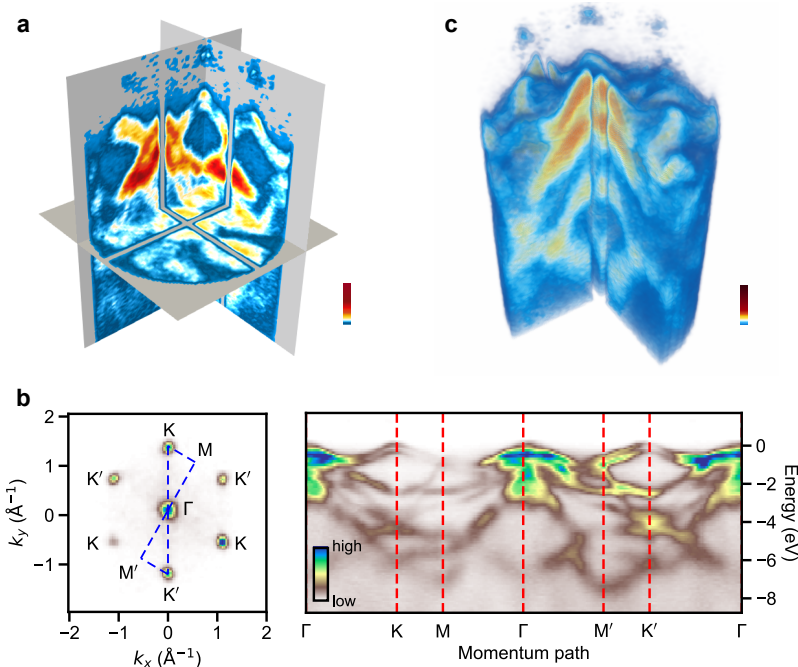


Figure 5: **Typical visual representations of the volumetric band mapping data.** The examples are illustrated using band mapping data of the layered semiconductor WSe_2 , measured with the HEXTOF instrument at FLASH and the METIS detector at the FHI (see Methods). The visualizations are presented in **a.** the orthoslice representation, **b.** the band path diagram (right) with the momentum path labelled in dashed blue line in the momentum k_x - k_y plane (left), and **c.** the cut-out view. The letters in **b** label the high symmetry points in the k_x - k_y plane (left) and along the momentum path (right) of the hexagonal Brillouin zone of WSe_2 [49].

Downstream analysis. Typical data analysis of PES data involves extracting electronic structure parameters, physical coupling constants and lifetimes via fitting of lineshapes [16] or dynamical models [50]. At the end of our distributed workflow, the data size is on the order of a few to tens of gigabytes, which can be directly loaded into memory on users' local machines, where downstream data analysis is carried out with custom routines.

2.4 Workflow archiving and reuse

The central goal of an open-source workflow is its reproducibility. We share the distributed workflow among users of the beamlines or facilities, its archiving allows transparent comparison between experimental runs and reuse for the simultaneous benefits of machine diagnostics and community-building. In our workflow, archiving of the workflow is achieved through storage of critical parameters generated during the workflow as workflow parameters (see Fig. 1), which include the numerical values used in binning, the intermediate parameters and coefficients of the correction and calibration functions. These stored parameters can be deployed in processing other datasets either in a notebook environment or in batch jobs run on consoles.

3 Discussion

We have designed and implemented an open-source distributed workflow for processing single-event data produced in recently established multidimensional photoemission spectroscopy based on a TOF 3D electron spectrometer. The workflow takes full advantage of the single-event data streams directly accessible from the TOF delay-line detector for event-wise correction and calibration and converts the raw events to the calibrated data hypervolume for project-specific downstream analysis. The functionalities within the workflow are publicly accessible through the open-source software packages we have developed (`hextof-processor` [31] and `mpes` [32]). The workflow also offers a route for archiving and is reusable partly or completely for batch processing similar datasets. The methods described here are applicable to all existing types of multidimensional photoemission band mapping measurements.

Open-sourcing the data workflow via publicly available softwares answers to the calls for open data and reproducible research in the materials science community [7, 8]. The open source software packages provide the basis for phased future extension and integration with existing analytical tools of the photoemission spectroscopy community. This is especially beneficial to photoemission spectroscopy since the interpretation of photoemission data is often linked to the observed or extracted outstanding features such as intensity local extrema, dispersion kinks and satellites, lineshape parameters and pattern symmetry [16]. Casting the workflow in the Python programming environment provides the foundation for convenient incorporation of existing image processing and machine-learning resources [51] for further exploration and understanding of the band mapping datasets, which are rich in information owing to the complex nature of the photoemission process [16, 19]. The modular structure of the packages introduced here allows well-paced and target-specific upgrades by both temporary and dedicated maintainers and users. Moreover, the potential integration with existing electronic structure-related softwares [5, 52, 53, 54] will facilitate the direct comparison between experimental results and theoretical calculations.

Methods

Sample preparation. Single-crystalline samples of 2D bulk WSe₂ were purchased from HQ Graphene. Crystals of size around 5 mm x 5 mm were used directly for the measurements. To prepare a clean surface by cleaving, we attached a cleaving pin upright to the sample surface using conducting epoxy (EPOTEC H20) outside the vacuum chamber and removed the pin by an abrupt motion in ultrahigh vacuum.

Photoemission experiments. The measurements were conducted using the HEXTOF instrument [25] at the DESY FLASH PG-2 beamline [55] with the free-electron laser (FEL) as well as an laboratory source [22] with a METIS electron momentum microscope (SPECS METIS 1000) constructed at the FHI. In all measurements at FLASH, the FEL was tuned to 36.5 eV (or 34.0 nm) and 109 eV, the optical pump pulse had a center wavelength of 775 nm. The measurements at the FHI used a 21.7 eV home-built extreme ultraviolet source based on high harmonic generation and driven by an optical parametric chirped-pulse amplifier (OPCPA) operating at 500 kHz repetition rate [56].

Author contributions

Y.A. and K.B. wrote the first version of the `hextof-processor` package, which was later improved by S.Y.A., D.C., R.P.X. and M.D.. R.P.X. wrote the `mpes` package with improvements from L.R.. D.K., Y.A., F.P., R.P.X., S.Y.A., D.C., M.D., M.H., S.D., L.R., R.E. and W.W. participated in the experiments at the FLASH PG-2 beamline using the HEXTOF instrument in Hamburg. S.D. and L.R. conducted the experiment at the Fritz Haber Institute using the METIS electron momentum microscope. R.P.X. wrote the initial manuscript with contributions from M.D. and Y.A. All authors contributed to the discussions and corrections to bring the manuscript to its final form.

Acknowledgement

We thank G. Schönhense for support on the photoelectron detector and S. Grunewald, S. Schülke and G. Schnapka for support on the computing infrastructures. We thank G. Brenner, H. Redlin and S. Dziarzhyski at FLASH, DESY, for beamline support. The work was partially supported by BiGmax, the Max Planck Society’s Research Network on Big-Data-Driven Materials-Science, the European Research Council (ERC) under the European Union’s Horizon 2020 research and innovation program (Grant No. ERC-2015-CoG-682843), and the German Research Foundation (DFG) through the Emmy Noether program under grant number RE 3977/1. F.P. acknowledges funding from the excellence cluster EXC 1074 “The Hamburg

Centre for Ultrafast Imaging - Structure, Dynamics and Control of Matter at the Atomic Scale” of the DFG. S.Y. Agustsson and J. Demsar acknowledge the financial support by the DFG in the framework of the Collaborative Research Centre SFB TRR 173 “Spin +X”.

References

- [1] C. Pruneau, *Data Analysis Techniques for Physical Scientists*, Cambridge University Press, 2017.
- [2] E. Deelman, T. Peterka, I. Altintas, C. D. Carothers, K. K. van Dam, K. Moreland, M. Parashar, L. Ramakrishnan, M. Taufer, J. Vetter, The future of scientific workflows, *The International Journal of High Performance Computing Applications* 32 (1) (2018) 159–175. doi:10.1177/1094342017704893.
- [3] A. Zakutayev, N. Wunder, M. Schwarting, J. D. Perkins, R. White, K. Munch, W. Tumas, C. Phillips, An open experimental database for exploring inorganic materials, *Scientific Data* 5 (1) (2018) 180053. doi:10.1038/sdata.2018.53.
- [4] L. Himanen, A. Geurts, A. S. Foster, P. Rinke, *Data-Driven Materials Science: Status, Challenges, and Perspectives*, *Advanced Science* (2019) 1900808doi:10.1002/advs.201900808.
- [5] G. Pizzi, A. Togo, B. Kozinsky, Provenance, workflows, and crystallographic tools in materials science: AiiDA, spglib, and seekpath, *MRS Bulletin* 43 (09) (2018) 696–702. doi:10.1557/mrs.2018.203.
- [6] J. M. Perkel, Workflow systems turn raw data into scientific knowledge, *Nature* 573 (7772) (2019) 149–150. doi:10.1038/d41586-019-02619-z.
- [7] J. Hill, G. Mulholland, K. Persson, R. Seshadri, C. Wolverton, B. Meredig, Materials science with large-scale data and informatics: Unlocking new opportunities, *MRS Bulletin* 41 (5) (2016) 399–409. doi:10.1557/mrs.2016.93.
- [8] C. Draxl, M. Scheffler, NOMAD: The FAIR concept for big data-driven materials science, *MRS Bulletin* 43 (09) (2018) 676–682. doi:10.1557/mrs.2018.208.
- [9] G. Schönhense, K. Medjanik, H.-J. Elmers, Space-, time- and spin-resolved photoemission, *Journal of Electron Spectroscopy and Related Phenomena* 200 (2015) 94–118. doi:10.1016/j.elspec.2015.05.016.
- [10] K. Medjanik, O. Fedchenko, S. Chernov, D. Kutnyakhov, M. Ellguth, A. Oelsner, B. Schönhense, T. R. F. Peixoto, P. Lutz, C.-H. Min, F. Reinert, S. Däster, Y. Acremann, J. Viefhaus, W. Wurth, H. J. Elmers, G. Schönhense, Direct 3D mapping

- of the Fermi surface and Fermi velocity, *Nature Materials* 16 (6) (2017) 615–621. doi:10.1038/nmat4875.
- [11] B. Schönhense, K. Medjanik, O. Fedchenko, S. Chernov, M. Ellguth, D. Vasilyev, A. Oelsner, J. Viefhaus, D. Kutnyakhov, W. Wurth, H. J. Elmers, G. Schönhense, Multidimensional photoemission spectroscopy—the space-charge limit, *New Journal of Physics* 20 (3) (2018) 033004. doi:10.1088/1367-2630/aaa262.
- [12] B. Krömker, M. Escher, D. Funnemann, D. Hartung, H. Engelhard, J. Kirschner, Development of a momentum microscope for time resolved band structure imaging, *Review of Scientific Instruments* 79 (5) (2008) 053702. doi:10.1063/1.2918133.
- [13] R. Ovsyannikov, P. Karlsson, M. Lundqvist, C. Lupulescu, W. Eberhardt, A. Föhlisch, S. Svensson, N. Mårtensson, Principles and operation of a new type of electron spectrometer – ArTOF, *Journal of Electron Spectroscopy and Related Phenomena* 191 (2013) 92–103. doi:10.1016/j.elspec.2013.08.005.
- [14] A. Damm, J. Gütde, P. Feulner, A. Czasch, O. Jagutzki, H. Schmidt-Böcking, U. Höfer, Application of a time-of-flight spectrometer with delay-line detector for time- and angle-resolved two-photon photoemission, *Journal of Electron Spectroscopy and Related Phenomena* 202 (2015) 74–80. doi:10.1016/j.elspec.2015.03.009.
- [15] C. Tusche, A. Krasnyuk, J. Kirschner, Spin resolved bandstructure imaging with a high resolution momentum microscope, *Ultramicroscopy* 159 (2015) 520–529. doi:10.1016/j.ultramicro.2015.03.020.
- [16] A. Damascelli, Z. Hussain, Z.-X. Shen, Angle-resolved photoemission studies of the cuprate superconductors, *Reviews of Modern Physics* 75 (2) (2003) 473–541. doi:10.1103/RevModPhys.75.473.
- [17] V. Strocov, Intrinsic accuracy in 3-dimensional photoemission band mapping, *Journal of Electron Spectroscopy and Related Phenomena* 130 (1-3) (2003) 65–78. doi:10.1016/S0368-2048(03)00054-9.
- [18] H. Yang, A. Liang, C. Chen, C. Zhang, N. B. M. Schroeter, Y. Chen, Visualizing electronic structures of quantum materials by angle-resolved photoemission spectroscopy, *Nature Reviews Materials* 3 (9) (2018) 341–353. doi:10.1038/s41578-018-0047-2.
- [19] S. Suga, A. Sekiyama, *Photoelectron Spectroscopy: Bulk and Surface Electronic Structures*, Springer, 2014.

- [20] M. Couprie, New generation of light sources: Present and future, *Journal of Electron Spectroscopy and Related Phenomena* 196 (2014) 3–13. doi:10.1016/j.elspec.2013.12.007.
- [21] C.-T. Chiang, M. Huth, A. Trüttschler, M. Kiel, F. O. Schumann, J. Kirschner, W. Widra, Boosting laboratory photoelectron spectroscopy by megahertz high-order harmonics, *New Journal of Physics* 17 (1) (2015) 013035. doi:10.1088/1367-2630/17/1/013035.
- [22] M. Puppin, Y. Deng, C. W. Nicholson, J. Feldl, N. B. M. Schröter, H. Vita, P. S. Kirchmann, C. Monney, L. Rettig, M. Wolf, R. Ernstorfer, Time- and angle-resolved photoemission spectroscopy of solids in the extreme ultraviolet at 500 kHz repetition rate, *Review of Scientific Instruments* 90 (2) (2019) 023104. doi:10.1063/1.5081938.
- [23] C. Corder, P. Zhao, J. Bakalis, X. Li, M. D. Kershis, A. R. Muraca, M. G. White, T. K. Allison, Ultrafast extreme ultraviolet photoemission without space charge, *Structural Dynamics* 5 (5) (2018) 054301. doi:10.1063/1.5045578.
- [24] J. H. Buss, H. Wang, Y. Xu, J. Maklar, F. Joucken, L. Zeng, S. Stoll, C. Jozwiak, J. Pepper, Y.-D. Chuang, J. D. Denlinger, Z. Hussain, A. Lanzara, R. A. Kaindl, A setup for extreme-ultraviolet ultrafast angle-resolved photoelectron spectroscopy at 50-kHz repetition rate, *Review of Scientific Instruments* 90 (2) (2019) 023105. doi:10.1063/1.5079677.
- [25] D. Kutnyakhov, R. P. Xian, M. Dendzik, M. Heber, F. Pressacco, S. Y. Agustsson, L. Wenthaus, H. Meyer, S. Gieschen, G. Mercurio, A. Benz, K. Bühlman, S. Däster, R. Gort, D. Curcio, K. Volckaert, M. Bianchi, C. Sanders, J. Miwa, S. Ulstrup, A. Oelsner, C. Tusche, Y.-J. Chen, D. Vasilyev, K. Medjanik, G. Brenner, S. Dziarzhyski, H. Redlin, B. Manschwetus, J. Hauer, S. Dong, L. Rettig, J. Demsar, H.-J. Elmers, P. Hofmann, R. Ernstorfer, G. Schönhense, Y. Acremann, W. Wurth, First time- and momentum-resolved photoemission studies using time-of-flight momentum microscopy at a free-electron laser [arXiv:1906.12155](https://arxiv.org/abs/1906.12155).
- [26] M. Folk, G. Heber, Q. Koziol, E. Pourmal, D. Robinson, An overview of the HDF5 technology suite and its applications, in: *Proceedings of the EDBT/ICDT 2011 Workshop on Array Databases - AD '11*, ACM Press, New York, New York, USA, 2011, pp. 36–47. doi:10.1145/1966895.1966900.
- [27] N. C. Weiler, F. Collman, J. T. Vogelstein, R. Burns, S. J. Smith, Synaptic molecular imaging in spared and deprived columns of mouse barrel cortex with array tomography, *Scientific Data* 1 (2014) 140046. doi:10.1038/sdata.2014.46.

- [28] D. F. E. Ker, S. Eom, S. Sanami, R. Bise, C. Pascale, Z. Yin, S.-i. Huh, E. Osuna-Highley, S. N. Junkers, C. J. Helfrich, P. Y. Liang, J. Pan, S. Jeong, S. S. Kang, J. Liu, R. Nicholson, M. F. Sandbothe, P. T. Van, A. Liu, M. Chen, T. Kanade, L. E. Weiss, P. G. Campbell, Phase contrast time-lapse microscopy datasets with automated and manual cell tracking annotations, *Scientific Data* 5 (2018) 180237. doi:10.1038/sdata.2018.237.
- [29] B. D. Levin, E. Padgett, C.-C. Chen, M. Scott, R. Xu, W. Theis, Y. Jiang, Y. Yang, C. Ophus, H. Zhang, D.-H. Ha, D. Wang, Y. Yu, H. D. Abruña, R. D. Robinson, P. Ercius, L. F. Kourkoutis, J. Miao, D. A. Muller, R. Hovden, Nanomaterial datasets to advance tomography in scanning transmission electron microscopy, *Scientific Data* 3 (2016) 160041. doi:10.1038/sdata.2016.41.
- [30] R. Aversa, M. H. Modarres, S. Cozzini, R. Ciancio, A. Chiusole, The first annotated set of scanning electron microscopy images for nanoscience, *Scientific Data* 5 (2018) 180172. doi:10.1038/sdata.2018.172.
- [31] Y. Acremann, K. Bühlmann, S. Y. Agustsson, D. Curcio, R. P. Xian, M. Dendzik, hextof-processor, <https://github.com/momentoscope/hextof-processor>.
- [32] R. P. Xian, L. Rettig, mpes, <https://github.com/mpes-kit/mpes>.
- [33] W. Ackermann, G. Asova, V. Ayvazyan, A. Azima, N. Baboi, J. Bähr, V. Balandin, B. Beutner, A. Brandt, A. Bolzmann, R. Brinkmann, O. I. Brovko, M. Castellano, P. Castro, L. Catani, E. Chiadroni, S. Choroba, A. Cianchi, J. T. Costello, D. Cubaynes, J. Dardis, W. Decking, H. Delsim-Hashemi, A. Delserieys, G. Di Pirro, M. Dohlus, S. Düsterer, A. Eckhardt, H. T. Edwards, B. Faatz, J. Feldhaus, K. Flöttmann, J. Frisch, L. Fröhlich, T. Garvey, U. Gensch, C. Gerth, M. Görler, N. Golubeva, H.-J. Grabosch, M. Grecki, O. Grimm, K. Hacker, U. Hahn, J. H. Han, K. Honkavaara, T. Hott, M. Hüning, Y. Ivanisenko, E. Jaeschke, W. Jalmuzna, T. Jezynski, R. Kammering, V. Katalev, K. Kavanagh, E. T. Kennedy, S. Khodyachykh, K. Klose, V. Kocharyan, M. Körfer, M. Kollwe, W. Koprek, S. Korepanov, D. Kostin, M. Krassilnikov, G. Kube, M. Kuhlmann, C. L. S. Lewis, L. Lilje, T. Limberg, D. Lipka, F. Löhl, H. Luna, M. Luong, M. Martins, M. Meyer, P. Michelato, V. Miltchev, W. D. Möller, L. Monaco, W. F. O. Müller, O. Napieralski, O. Napoly, P. Nicolosi, D. Nölle, T. Nuñez, A. Oppelt, C. Pagani, R. Paparella, N. Pchalek, J. Pedregosa-Gutierrez, B. Petersen, B. Petrosyan, G. Petrosyan, L. Petrosyan, J. Pflüger, E. Plönjes, L. Poletto, K. Pozniak, E. Prat, D. Proch, P. Pucyk, P. Radcliffe, H. Redlin, K. Rehlich, M. Richter, M. Roehrs, J. Roensch, R. Romaniuk, M. Ross, J. Rossbach, V. Rybnikov, M. Sachwitz, E. L. Saldin, W. Sandner, H. Schlarb, B. Schmidt, M. Schmitz, P. Schmüser, J. R. Schneider, E. A. Schneidmiller,

- S. Schnepp, S. Schreiber, M. Seidel, D. Sertore, A. V. Shabunov, C. Simon, S. Simrock, E. Sombrowski, A. A. Sorokin, P. Spanknebel, R. Spesyvtsev, L. Staykov, B. Steffen, F. Stephan, F. Stulle, H. Thom, K. Tiedtke, M. Tischer, S. Toleikis, R. Treusch, D. Trines, I. Tsakov, E. Vogel, T. Weiland, H. Weise, M. Wellhöfer, M. Wendt, I. Will, A. Winter, K. Wittenburg, W. Wurth, P. Yeates, M. V. Yurkov, I. Zagorodnov, K. Zapfe, Operation of a free-electron laser from the extreme ultraviolet to the water window, *Nature Photonics* 1 (6) (2007) 336–342. doi:10.1038/nphoton.2007.76.
- [34] Dask Development Team, Dask: Library for dynamic task scheduling (2016).
URL <https://dask.org>
- [35] T. White, Hadoop : the definitive guide, 4th Edition, O’Reilly Media, 2015.
- [36] M. Chambers, S. Cleveland, A. Tukey, B. Kleiner, Graphical Methods for Data Analysis, Wadsworth International Group, 1983.
- [37] D. Novo, J. Wood, Flow cytometry histograms: Transformations, resolution, and display, *Cytometry Part A* 73A (8) (2008) 685–692. doi:10.1002/cyto.a.20592.
- [38] R. P. Xian, L. Rettig, R. Ernstorfer, Symmetry-guided nonrigid registration: The case for distortion correction in multidimensional photoemission spectroscopy, *Ultramicroscopy* 202 (2019) 133–139. doi:10.1016/j.ultramicro.2019.04.004.
- [39] M. Guizar-Sicairos, S. T. Thurman, J. R. Fienup, Efficient subpixel image registration algorithms, *Optics Letters* 33 (2) (2008) 156. doi:10.1364/OL.33.000156.
- [40] P. Viola, W.M.Wells, Alignment by Maximisation of Mutual Information, *International Journal of Computer Vision* 24 (2) (1997) 137–154. doi:10.1023/A:1007958904918.
- [41] S. Salvador, P. Chan, Toward accurate dynamic time warping in linear time and space, *Intelligent Data Analysis* 11 (5) (2007) 561–580.
- [42] C. D. Hansen, C. R. Johnson (Eds.), *The Visualization Handbook*, Elsevier Butterworth-Heinemann, 2005.
- [43] D. R. Lipsa, R. S. Laramee, S. J. Cox, J. C. Roberts, R. Walker, M. A. Borkin, H. Pfister, Visualization for the Physical Sciences, *Computer Graphics Forum* 31 (8) (2012) 2317–2347. doi:10.1111/j.1467-8659.2012.03184.x.
- [44] J. D. Hunter, Matplotlib: A 2d graphics environment, *Computing in Science & Engineering* 9 (3) (2007) 90–95. doi:10.1109/MCSE.2007.55.

- [45] B. O. Community, Blender - a 3D modelling and rendering package, Blender Foundation, Stichting Blender Foundation, Amsterdam (2018).
URL <http://www.blender.org>
- [46] M. Dendzik, 4Dview (2019). doi:10.5281/zenodo.3360817.
- [47] W. Setyawan, S. Curtarolo, High-throughput electronic band structure calculations: Challenges and tools, *Computational Materials Science* 49 (2) (2010) 299–312. doi:10.1016/j.commatsci.2010.05.010.
- [48] Y. Hinuma, G. Pizzi, Y. Kumagai, F. Oba, I. Tanaka, Band structure diagram paths based on crystallography, *Computational Materials Science* 128 (2017) 140–184. doi:10.1016/j.commatsci.2016.10.015.
- [49] J. M. Riley, F. Mazzola, M. Dendzik, M. Michiardi, T. Takayama, L. Bawden, C. Granerød, M. Leandersson, T. Balasubramanian, M. Hoesch, T. K. Kim, H. Takagi, W. Meevasana, P. Hofmann, M. S. Bahramy, J. W. Wells, P. D. C. King, Direct observation of spin-polarized bulk bands in an inversion-symmetric semiconductor, *Nature Physics* 10 (11) (2014) 835–839. doi:10.1038/nphys3105.
- [50] M. Weinelt, Time-resolved two-photon photoemission from metal surfaces, *Journal of Physics: Condensed Matter* 14 (43) (2002) R1099–R1141. doi:10.1088/0953-8984/14/43/202.
- [51] K. T. Butler, D. W. Davies, H. Cartwright, O. Isayev, A. Walsh, Machine learning for molecular and materials science, *Nature* 559 (7715) (2018) 547–555. doi:10.1038/s41586-018-0337-2.
- [52] S. P. Ong, W. D. Richards, A. Jain, G. Hautier, M. Kocher, S. Cholia, D. Gunter, V. L. Chevrier, K. A. Persson, G. Ceder, Python Materials Genomics (pymatgen): A robust, open-source python library for materials analysis, *Computational Materials Science* 68 (2013) 314–319. doi:10.1016/j.commatsci.2012.10.028.
- [53] A. Hjorth Larsen, J. Jørgen Mortensen, J. Blomqvist, I. E. Castelli, R. Christensen, M. Dułak, J. Friis, M. N. Groves, B. Hammer, C. Hargus, E. D. Hermes, P. C. Jennings, P. Bjerre Jensen, J. Kermode, J. R. Kitchin, E. Leonhard Kolsbjerg, J. Kubal, K. Kaasbjerg, S. Lysgaard, J. Bergmann Maronsson, T. Maxson, T. Olsen, L. Pastewka, A. Peterson, C. Rostgaard, J. Schiøtz, O. Schütt, M. Strange, K. S. Thygesen, T. Vegge, L. Vilhelmsen, M. Walter, Z. Zeng, K. W. Jacobsen, The atomic simulation environment—a Python library for working with atoms, *Journal of Physics: Condensed Matter* 29 (27) (2017) 273002. doi:10.1088/1361-648X/aa680e.

- [54] A. M. Ganose, A. J. Jackson, D. O. Scanlon, sumo: Command-line tools for plotting and analysis of periodic ab initio calculations, *Journal of Open Source Software* 3 (28) (2018) 717. doi:10.21105/joss.00717.
- [55] N. Gerasimova, S. Dziarzhytski, J. Feldhaus, The monochromator beamline at FLASH: performance, capabilities and upgrade plans, *Journal of Modern Optics* 58 (16) (2011) 1480–1485. doi:10.1080/09500340.2011.588344.
- [56] M. Puppin, Y. Deng, O. Prochnow, J. Ahrens, T. Binhammer, U. Morgner, M. Krenz, M. Wolf, R. Ernstorfer, 500 kHz OPCPA delivering tunable sub-20 fs pulses with 15 W average power based on an all-ytterbium laser, *Optics Express* 23 (2) (2015) 1491. doi:10.1364/OE.23.001491.